https://doi.org/10.1007/s41230-024-3127-5

Phase-field lattice-Boltzmann study on fully coupled thermal-solute-convection dendrite growth of Al-Cu alloy

Yin-qi Qiu[1], *Meng-wu Wu[1, 2], Xun-peng Qin[2], and Shou-mei Xiong[3]

1. Hubei Key Laboratory of Advanced Technology for Automotive Components, Wuhan University of Technology, Wuhan 430070, China

2. Hubei Longzhong Laboratory, Xiangyang 441000, Hubei, China

3. School of Materials Science and Engineering, Tsinghua University, Beijing 100084, China

Abstract: Dendrite growth is a complex liquid-solid phase transition process involving multiple physical factors. A phase-field lattice-Boltzmann method was developed to simulate the two- and three-dimension dendrite growth of Al-Cu alloy. The effect of fully coupled thermal-solute-convection interaction on the dendrite growth was investigated by incorporating a parallel-adaptive mesh refinement algorithm into the numerical model. By accurately reproducing the latent heat release, solute diffusion and convective transport behaviors at the liquid-solid interface, the interaction mechanism among thermal-solute-convection transport as well as their coupling effects on the dendrite growth dynamics were discussed. The simulation results show that the release of latent heat slows down the dendrite growth rate, and both natural and forced convection disrupt the symmetrical growth of dendrites. Their combination makes the growth of dendrites more complex, capturing important physical aspects such as recalescence, dendrite tip splitting, dendrite tilting, dendrite remelting, and solute plume in the simulation case. Based on the robustness and powerful ability of the numerical model, the formation mechanisms of these physical aspects were revealed.

Keywords: simulation; phase field; dendrite growth; thermal-solute-convection interaction

CLC numbers: TG146.21/TP391.9 **Document code:** A **Article ID:** 1672-6421(2024)02-125-12

1 Introduction

Metal solidification is a fundamental phenomenon in casting, welding and additive manufacturing processes, and it has an important impact on the properties of alloys [1]. Dendrite growth is ubiquitous during metal alloy solidification due to the instability of the solid-liquid interface triggered by thermal or solute disturbance [2-3]. In the actual metal solidification process, there is a wide range of heat-mass-flow interaction, enriching the diversity of dendrite growth morphology, which in turn affects the metal alloy solidification structure and the formation of defects such as solute segregation, shrinkage and porosity, etc. [4-5]. Various experimental methods, for example, scanning electronic microscopy (SEM), transmission electron microscopy (TEM), X-ray synchrotron radiation technique, neutron diffraction technique, etc., have improved understanding of the metal solidification process [6-9]. In particular, the rapid development of X-ray synchrotron radiation technique has already enabled real-time photographic observation of dendrite growth. However, the multi-scale, high temperature and transient nature of alloy solidification process, and the complexity induced by the thermal-solute-convection interaction increase the difficulty of in-situ observation [10]. Since the experimental conditions are prone to be disturbed and the experimental parameters are not easy to be accurately controlled, there are still difficulties in quantitatively distinguishing the effects of various influencing factors on dendrite growth by experiments.

In recent years, the rapid development and application of microstructure simulation technology have compensated for the shortage of experimental

***Meng-wu Wu**

Male, Ph. D., Professor. His research interests mainly focus on lightweight design of automobiles and advanced manufacturing technologies for automotive components.

E-mail: wumw@whut.edu.cn

Received: 2023-10-06; Accepted: 2024-01-30

characterization methods. This is reflected in the fact that microstructure simulation can accurately depict the time-dependent microstructure evolution during alloy solidification and effectively predict microstructure characteristics, showing great advantages in the study of alloy solidification process [11-13]. As one of the most popular numerical simulation methods, the phase field (PF) method has unique advantages in describing phase transition and dendrite growth, making it a hotspot and main development direction in the field of microstructure simulation [14-16]. Based on thermodynamic consistency, the phase field method can recover the Gibbs-Thomson effect and simulate interface dynamics with high accuracy. By introducing an order parameter, namely phase field φ, the phase field method avoids explicitly tracking of the liquid-solid interface.

Since the actual metal solidification involves complex thermal-solute-convection interaction, investigation on dendrite growth by the phase field method has gone through the development process from single- to multiple-physics modeling. During this period, Warren et al. [17, 18] took account of the latent heat release in the simulation on dendrite growth of a binary alloy for the first time, and described the recalescence phenomenon during metal solidification. Ramirez et al. [19, 20] developed a phase field model for quantitatively simulating dendrite growth with coupled heat and solute diffusion, in which both the solute anti-trapping and latent heat release were taken into account. Combining the phase field model with a parallel-adaptive mesh refinement (Para-AMR) algorithm, Zhang et al. [21] studied the effect of latent heat release on the three-dimension dendrite growth of Al-Cu alloy, and found that dendrites were different in morphology due to the uneven temperature caused by the latent heat release. As for simulation works on dendrite growth with coupled solute diffusion and melt convection, Tönhardt et al. [22, 23] were among the first to utilize the phase field method to study the effect of melt convection on dendrite growth, and found that the growth of dendrite arms at the upstream side was promoted, while the growth of dendrite arms on the downstream was suppressed. Beckermann et al. [24-26] systematically investigated the influence of flow velocity and direction, as well as the interfacial energy anisotropy on dendrite growth morphology, and compared the phase field simulation results with the linearized solvability theory, and the results were consistent. To overcome the divergence problem of the calculation program when solving the Navier-Stokes equations of the melt with a high volume fraction of solid, Miller et al. [27, 28] combined the lattice-Boltzmann method (LBM) with the phase field model for the first time to study dendrite growth with coupled solute diffusion and melt convection. Their work is a milestone in the field of microstructure simulation. Since then, the LBM has been widely used to solve momentum and energy transport problems, showing great advantages such as high calculation accuracy, superior convergence, and low computational cost. Recently, Ohno et al. [29] and Zhang et al. [30] studied the effect of natural convection on dendrite morphology during directional solidification of a binary alloy by using a coupled PF-LBM approach. They reported the formation of chimney-like or mushroom-like solute plumes when the dendrites grew along the gravitational direction.

Up to date, plenty of simulation works have been carried out on dendrite growth with coupled solute diffusion and thermal transport, or coupled solute diffusion and melt convection. However, for the fully coupled thermal-solute-convection transport, very limited studies are performed. The reason is that the thermal diffusion coefficient and kinematic viscosity are generally two and four orders of magnitude greater than the solute diffusion coefficient in liquid for metallic alloys, respectively [31]. When solving the fully coupled thermal-solute-convection problem, the discrete time step of the numerical model will be four orders of magnitude smaller than that used for pure solute diffusion condition. Consequently, the computational efficiency is greatly reduced [31]. More advanced computing architecture is needed to tackle the multiscale and multiphysical problems. Meanwhile, an accurate dendrite growth prediction requires a rigor physical model to characterize complex nonlinear dynamics during solidification, including the latent heat release, melt flow, solute redistribution, interfacial Gibbs-Thomson effect and dendrite anisotropy, etc. By introducing an adaptive finite volume method into the phase field model, Lan et al. [32] studied thermosolutal growth dynamics of a half dendrite under a forced flow. Guo et al. [33] and Zhang et al. [34] adopted a Para-AMR approach to reduce the computational overhead, allowing for some meaningful explorations into dendrite growth under fully coupled thermal-solute-convection condition.

In the present work, a robust PF-LBM model was developed to simulate the dendrite growth of Al-Cu alloy with fully coupled thermal-solute-convection interaction. A Para-AMR algorithm was then used to handle the enormous amount of data and improve the computing efficiency of the numerical model. 2D and 3D simulation cases were performed to investigate the internal relations between various physical fields and their coupling effect on the dendrite growth. Based on the simulation results, several important physical aspects relating to dendrite growth were discussed as well.

2 Numerical model

2.1 Phase-field model for dendrite growth

The phase field model for dendrite growth was established according to the energy functional theory, which assumed that the total free energy of the system included two parts, the interface free energy and the volume free energy. The total free energy E is then expressed as a function of three variables, including the phase field φ, solute concentration C and temperature T. Consequently, the evolution of these three variables over time can be obtained by calculating the variation of the total free energy of the system on the corresponding variables. The specific governing equations are given by [35]:

$$E(\varphi,C,T)=\int\left[\frac{\sigma}{2}|\nabla\varphi|^2+f_{\mathrm{AB}}(\varphi,C,T)\right]\mathrm{d}V \quad (1)$$

$$\frac{\partial \varphi}{\partial t}=-K_{\varphi}\frac{\delta E}{\delta \varphi} \tag{2}$$

$$\frac{\partial C}{\partial t}+f_1 v\cdot\nabla C=\nabla\cdot\left(K_C\nabla\frac{\delta E}{\delta C}-j_{at}\right) \tag{3}$$

$$\frac{\partial T}{\partial t}+f_1 v\cdot\nabla T=\alpha_t\nabla^2 T-\frac{L}{2c_p}\frac{\partial f_1}{\partial t}-\dot{q} \tag{4}$$

where φ varies smoothly from −1 (liquid phase) to 1 (solid phase). When taking a value between −1 and 1, it represents the solid-liquid interface. σ is the gradient energy coefficient. f_{AB} denotes the bulk free energy density of a dilute binary alloy containing components A and B. $f_l=(1-\varphi)/2$ is the fraction of liquid phase. v is the flow velocity. K_φ and K_C are constants. j_{at} represents an anti-trapping current [36], which is non-zero only at the solid-liquid interface to eliminate the non-equilibrium effect at the diffuse interface. α_t is the thermal diffusion coefficient. L denotes the latent heat and c_p is the specific heat capacity. $\dot{q}>0$ is a cooling term to simulate the temperature drop in the computational domain.

Dimensionless solute concentration U_{PF}, dimensionless undercooling θ_{PF}, dimensionless time t_{PF} and dimensionless length x_{PF} are defined as [37]:

$$t_{PF}=t/\tau_0 \tag{5}$$

$$x_{PF}=x/W_0 \tag{6}$$

$$U_{PF}=\frac{\dfrac{2C/C_\infty}{1+k-(1-k)\varphi}-1}{1-k} \tag{7}$$

$$\theta_{PF}=\frac{T-mC_\infty-T_M}{\Delta T_0} \tag{8}$$

where $\tau_0=d_c^2 a_2\lambda_{cp}^3/\left(Da_1^2\right)$ and $W_0=\lambda_{cp}d_c/a_1$ are the time and length bases from the real to the phase field unit, respectively. D is the solute diffusion coefficient. C_∞ is the far-field solute concentration. In other words, C_∞ denotes the initial solute concentration. k is the equilibrium solute partition coefficient. T_M is the melting point of the pure solvent. m is the liquidus slope. a_1=0.8839 and a_2=0.6267. $d_c=\Gamma/\Delta T_0$ is the chemical capillary length, and Γ is the Gibbs-Thomson coefficient. $\Delta T_0=|m|C_\infty(1-k)/k$ is the equilibrium freezing temperature range. λ_{cp} is the coupling parameter and defined as [37]:

$$\lambda_{cp}=\frac{15R_g T_M(1-k)}{16V_M e_b|m|}\Delta T_0 \tag{9}$$

where R_g, V_M and e_b are the gas constant, the molar volume, and the dimensionless energy barrier of the double well potential, respectively. Accordingly, the governing equations for phase field (dendrite anisotropy) can be finally espressed as:

$$\begin{aligned}&A(n)^2\left[\frac{1}{Le}+k\left(1+(1-k)U_{PF}\right)\right]\frac{\partial\varphi}{\partial t_{PF}}\\&=\frac{1}{2}\nabla\cdot\left[\frac{\partial\left(A(n)^2|\nabla\varphi|^2\right)}{\partial\nabla\varphi}\right]+\varphi-\varphi^3-\lambda_{cp}\left(1-\varphi^2\right)^2\left(\theta_{PF}+kU_{PF}\right)\end{aligned} \tag{10}$$

$$\begin{aligned}&\frac{1+k-(1-k)\varphi}{2}\frac{\partial U_{PF}}{\partial t_{PF}}=\nabla\cdot\left(D\frac{1-\varphi}{2}\nabla U_{PF}-j_{at}\right)\\&+\frac{1+(1-k)U_{PF}}{2}\frac{\partial\varphi}{\partial t_{PF}}-\frac{1}{2}v\cdot\left\{\left[1+k-(1-k)\varphi\right]\nabla U_{PF}\right.\\&\left.-\left[1+(1-k)U_{PF}\right]\nabla\varphi\right\}\end{aligned} \tag{11}$$

$$\frac{\partial\theta_{PF}}{\partial t_{PF}}+\frac{1-\varphi}{2}v\cdot\nabla\theta_{PF}=\alpha_t\nabla^2\theta_{PF}+\frac{1}{2}\frac{L/c_p}{\Delta T_0}\frac{\partial\varphi}{\partial t_{PF}}-\dot{q} \tag{12}$$

where Le is the Lewis number, i.e., $Le=\alpha_t/D$. For alloys with cubic dendrite structure, the interfacial anisotropy function A(n) in 2D case is given by [38]:

$$A(n)=1+\varepsilon\cos 4\theta \tag{13}$$

where ε is the anisotropy strength and θ denotes the angle between the normal of solid-liquid interface and the x-axis. For the 3D case, A(n) is expressed as [39]:

$$A(n)=1+\varepsilon_1(R-3/5)+\varepsilon_2(3R+66S-17/7) \tag{14}$$

$$R=\frac{\varphi_x^4+\varphi_y^4+\varphi_z^4}{|\nabla\varphi|^4} \tag{15}$$

$$S=\frac{\varphi_x^2\varphi_y^2\varphi_z^2}{|\nabla\varphi|^6} \tag{16}$$

where $\varphi_i=\partial\varphi/\partial i\,(i=x,y,z)$, ε_1 and ε_2 are the weight coefficients along the <100> and <110> dendrite growth directions, respectively.

2.2 Lattice-Boltzmann method for thermal-convection transport

As a mesoscopic kinetic method, the LBM regards the evolution of a macroscopic physical system as the movement of a series of particles. Then, the distribution function is the most important part of LBM as it is used to depict the motion characteristics of particles. The expression form of the distribution function, namely the Boltzmann transport equation, is as follows [40]:

$$\frac{\partial f}{\partial t}+c\cdot\nabla f=\Omega \tag{17}$$

where f is the distribution function, c is the lattice velocity, and Ω is the source term. According to the approximation of the Bhatnagar-Gross-Krook (BGK) model, Ω is expressed as [41]:

$$\Omega=\omega\left(f^{eq}-f\right)=\frac{1}{\tau}\left(f^{eq}-f\right) \tag{18}$$

where ω is the collision frequency between the lattices, τ is the relaxation factor, and f^{eq} is the equilibrium distribution function.

By substituting the approximate solution of Ω into the original equation and discretizing, the LBM equations governing the evolution of flow velocity and temperature can be given by [42]:

$$\begin{aligned}&f_i\left(r_{LB}+\delta r_{LB},t_{LB}+\delta t_{LB}\right)=f_i\left(r_{LB},t_{LB}\right)\\&-\frac{1}{\tau_f}\left[f_i\left(r_{LB},t_{LB}\right)-f_i^{eq}\left(r_{LB},t_{LB}\right)\right]+\delta t_{LB}F_i\end{aligned} \tag{19}$$

$$g_i\left(r_{\mathrm{LB}}+\delta r_{\mathrm{LB}},t_{\mathrm{LB}}+\delta t_{\mathrm{LB}}\right)=g_i\left(r_{\mathrm{LB}},t_{\mathrm{LB}}\right)-\frac{1}{\tau_g}\left[g_i\left(r_{\mathrm{LB}},t_{\mathrm{LB}}\right)-g_i^{\mathrm{eq}}\left(r_{\mathrm{LB}},t_{\mathrm{LB}}\right)\right]+\delta t_{\mathrm{LB}}G_i \quad (20)$$

$$f_i^{\mathrm{eq}}=\rho_{\mathrm{LB}}w_i\left[1+\frac{3e_i\cdot v_{\mathrm{LB}}}{c^2}+\frac{9\left(e_i\cdot v_{\mathrm{LB}}\right)^2}{2c^4}-\frac{3v_{\mathrm{LB}}\cdot v_{\mathrm{LB}}}{2c^2}\right] \quad (21)$$

$$g_i^{\mathrm{eq}}=\theta_{\mathrm{LB}}w_i\left[1+\frac{3e_i\cdot v_{\mathrm{LB}}}{c^2}+\frac{9\left(e_i\cdot v_{\mathrm{LB}}\right)^2}{2c^4}-\frac{3v_{\mathrm{LB}}\cdot v_{\mathrm{LB}}}{2c^2}\right] \quad (22)$$

where $f_i(r_{\mathrm{LB}},t_{\mathrm{LB}})$ and $g_i(r_{\mathrm{LB}},t_{\mathrm{LB}})$ are the particle distribution functions of flow velocity and temperature at the lattice site r_{LB} and discrete time t_{LB}, respectively. f_i^{eq} and g_i^{eq} are the corresponding equilibrium distribution functions. $\rho_{\mathrm{LB}}=\sum_i f_i$ and $\theta_{\mathrm{LB}}=\sum_i g_i$ are the particle densities of the solute equilibrium equation and the temperature equilibrium equation, respectively. e_i is the discrete velocity along the ith direction, and w_i is the corresponding weight coefficient. For 2D and 3D cases, the specific values of e_i and w_i can be referred to Ref. [37]. v_{LB} is the flow velocity in the LBM unit. $c=\delta r_{\mathrm{LB}}/\delta t_{\mathrm{LB}}$ is the lattice velocity, in which δr_{LB} and δt_{LB} are the lattice spacing step and time step, respectively in the LBM. τ_f and τ_g are the relaxation time related to the kinematic viscosity υ_{LB} and thermal diffusivity α_{LB}. They can be defined as [44]:

$$\tau_f=\frac{3\upsilon_{\mathrm{LB}}}{c^2\delta t_{\mathrm{LB}}}+0.5 \quad (23)$$

$$\tau_g=\frac{3\alpha_{\mathrm{LB}}}{c^2\delta t_{\mathrm{LB}}}+0.5 \quad (24)$$

F_i in Eq. (19) denotes the force driving the liquid flow, and G_i in Eq. (20) represents the heat source term such as the release of latent heat and forced cooling. They can be given by [44]:

$$F_i=\left(1-\frac{1}{2\tau_f}\right)w_i\left[\frac{3\left(e_i-v_{\mathrm{LB}}\right)}{c^2}+\frac{9\left(e_i\cdot v_{\mathrm{LB}}\right)e_i}{c^4}\right]\cdot\left(F_{\mathrm{d}}+F_{\mathrm{b}}\right) \quad (25)$$

$$G_i=\left(1-\frac{1}{2\tau_g}\right)w_i\left(\frac{1}{2}\frac{L/c_{\mathrm{p}}}{\Delta T_0}\frac{\partial\varphi}{\partial t_{\mathrm{LB}}}-\dot{q}\right) \quad (26)$$

where F_{d} and F_{b} are the interfacial drag force and the body force, respectively. Their specific expression form can be found in Ref. [45]. By the way shown in Eqs. (25–26), fully coupling of the phase field, solute concentration, temperature and flow velocity is achieved in the PF-LBM model.

2.3 Para-AMR algorithm and PF-LBM calculation process

To simulate dendrite growth with fully coupled thermal-solute-convection interaction, a Para-AMR algorithm developed by Guo et al. [33-34] was used to handle the enormous amount of data and improve the computing efficiency of the numerical model. The algorithm consists of two parts, adaptive meshing and parallel computing. The basis of adaptive meshing is that all variables (such as phase field, solute concentration, temperature and flow velocity) change the fastest at the solid-liquid interface. Therefore, sufficiently fine meshes are required at the solid-liquid interface to ensure the calculation accuracy of the numerical model, while coarse meshes can be used far from the interface. By this means, the scale of data calculation can be greatly reduced and the computing efficiency is then improved. It is worth mentioning that with the movement and evolution of the solid-liquid interface, the mesh size distribution of the calculation domain must be dynamically adjusted. Thus, a gradient criterion was used to realize dynamic meshing and finding meshes to be coarsened or refined [46]:

$$\left|\nabla\varphi\right|+\beta_{\mathrm{U}}\left|\nabla U_{\mathrm{PF}}\right|+\beta_\theta\left|\nabla\theta_{\mathrm{PF}}\right|+\beta_v\sqrt{\left|\nabla u_{\mathrm{PF}}\right|^2+\left|\nabla v_{\mathrm{PF}}\right|^2+\left|\nabla w_{\mathrm{PF}}\right|^2}\geq\xi \quad (27)$$

where u_{PF}, v_{PF} and w_{PF} are the flow velocity components. β_{U}, β_θ and β_v are the weight coefficients for the dimensionless solute concentration, undercooling and flow velocity, respectively. ξ is a threshold value, which is determined by numerical tests. Parallel computing is to divide computing tasks into multiple subtasks, and then use multi-core and multithreading to achieve parallel computing. During this period, message passing interface (MPI) technology was adopted to dispatch data among different parallel processors. By combining the parallel computing technology with the adaptive mesh refinement method, the Para-AMR algorithm is able to optimize the computing resources allocation and improve the computing efficiency. In particular, the time step can be magnified when a multi-layer mesh architecture was adopted in the PF-LBM model, resulting in a further improvement of the computing efficiency. As for the matching rules of the spacing step and time step between the PF and LBM, as well as among different physical problems such as phase field, solute concentration, temperature, and flow velocity, more details can be referred to Ref. [47].

As mentioned above, the phase field method was used to simulate the microscopic dendrite structure evolution, and the LBM was employed to calculate the heat transfer and melt flow in the two-phase region. Coupling of the PF and LBM solutions was schemed to realize simulation on dendrite growth with fully coupled thermal-solute-convection interaction. Figure 1 shows the computational flowchart of the PF-LBM model.

3 Simulation results and discussion

The Al-Cu alloy was selected in this work and the main thermo-physical parameters used for simulations are listed in Table 1. For simplicity, all parameters were set as constants. The melt was supposed to be the incompressible Newtonian fluid under convection. Since multi-physics problems needed to be solved in the numerical model, different boundary conditions were set accordingly.

For the simulation on equiaxed dendrite growth, all boundaries were set as outlet boundaries for both the solute field and temperature field, while different boundary conditions were set for different types of melt flow. In the case

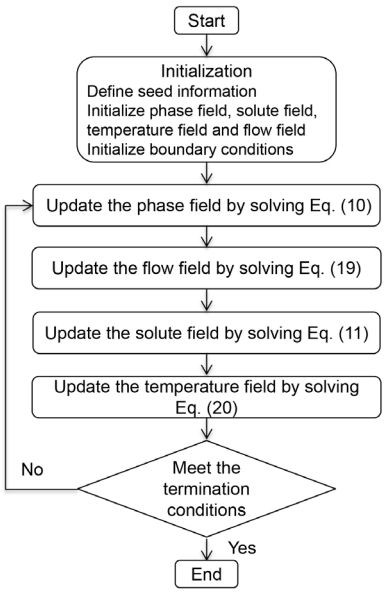

Fig. 1: Computational flowchart of PF-LBM model

of forced convection, the left boundary was the inlet boundary, the right boundary was the outlet boundary, and the other boundaries were no-slip boundaries. Under natural convection, all boundaries were set as no-slip boundaries for the flow field. For the simulation on columnar dendrite growth, the left and right boundaries of the computational domain were subjected to periodic boundary conditions for all variables, the other boundaries were set as outlet boundaries for the solute field and temperature field, and no-slip boundaries for the flow field. In addition, since the melt cannot pass through the dendrites, the solid-liquid interface was considered to be the no-slip and no-diffusion boundary using the bounce-back rule for flow field and solute field simulation. As for the grid size, since the adaptive meshing technology was used, the number of grid levels was 3 in 2D simulation cases, the finest and coarsest grid sizes were 0.8 and 3.2, respectively. In 3D simulations cases, the number of grid levels was 5, while the finest grid size was 0.8 and the coarsest grid size was 12.8.

Table 1: Physical parameters of Al-Cu alloy used in the present study [48, 49]

Definition and unit	Symbol	Value
Initial solute concentration in liquid phase (wt.%)	C_∞	4
Melting point of the pure solvent (K)	T_M	934
Liquidus slope (K·wt.%$^{-1}$)	m	−2.6
Equilibrium solute partition coefficient	k	0.15
Solute diffusion coefficient in solid (m^2·s^{-1})	D_s	3×10^{-12}
Solute diffusion coefficient in liquid (m^2·s^{-1})	D_l	3×10^{-9}
Thermal diffusion coefficient (m^2·s^{-1})	α_t	3×10^{-5}
Specific heat capacity (J·K^{-1}·kg^{-1})	c_p	1,050
Latent heat (J·kg^{-1})	L	3.814×10^5
Gibbs-Thomson coefficient (K·m)	Γ	2.4×10^{-7}
Density (kg·m^{-3})	ρ	2,475
Gravitational acceleration (m·s^{-2})	g	9.8

3.1 Single equiaxed dendrite growth

Figure 2 shows the dendrite growth dynamics and morphology of a single equiaxed dendrite growth under the pure solute diffusion, thermal-solute coupling and thermal-solute-convection coupling conditions. The size of the calculation domain was 1,638.4×1,638.4. The dimensionless temperature, T_{PF} (T_{PF}=1−θ_{PF}) was initially set to 0.7. To take the convection effect into account, an indicator named the solute expansion coefficient, β_c, was used to describe the density difference between the alloying element (solute) and the melt. Consequently, gravity-driven natural convection is then triggered. In this study, the gravitational direction is defined always vertical downward, and β_c<0 represents the solute Cu is heavier than the melt. In the simulation case of Fig. 2(c), β_c is set to −0.1.

It can be seen from Fig. 2 that there are significant differences in the dendrite growth dynamics and morphology with the same initial conditions on the solute and temperature fields. Under pure solute diffusion, dendrites exhibit a quadruple symmetric morphology and dense secondary dendrite arms [Fig. 2(a)]. In this case, the temperature of the computational domain remains consistent with the initial state, as illustrated in Fig. 2(d). Under thermal-solute coupling, it can be noted from Fig. 2(e) that the temperature of the melt near the solid-liquid interface increases rapidly due to the release of latent heat accompanied with the liquid to solid phase transformation. In other words, the recalescence phenomenon occurs in the melt in front of the solidification interface. Comparing Fig. 2(b) with Fig. 2(e), it can be seen that since the thermal diffusion coefficient is generally four orders of

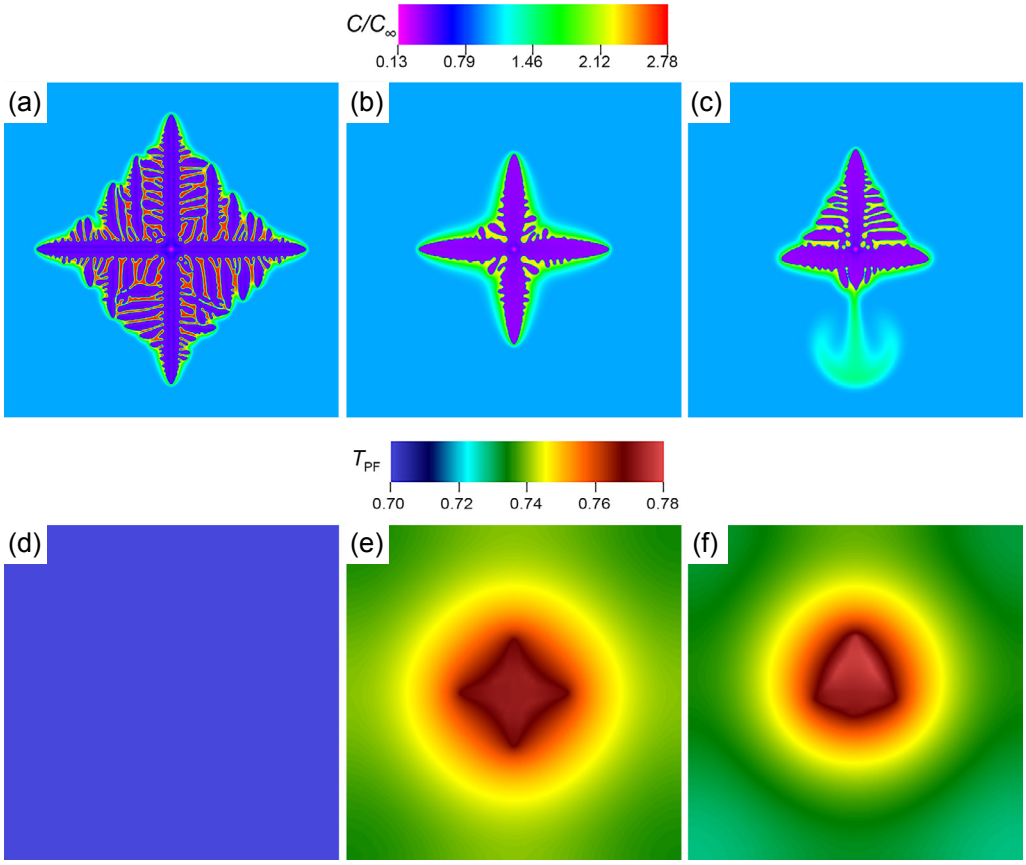

Fig. 2: Simulated solute field (a–c) and the corresponding temperature field (d–f) at the same time (6,000 steps) of a single equiaxed dendrite growth under pure solute diffusion (a, d), thermal-solute coupling (b, e), and thermal-solute-convection coupling (c, f)

magnitude greater than the solute diffusion coefficient in liquid, the thermal diffusion layer is much thicker than the solute diffusion layer. Meanwhile, the dendrites still have a perfect quadruple symmetric morphology, but their growth rate is much slower than that under pure solute diffusion conditions. That is to say, the release of latent heat affects the dendrite growth dynamics remarkably by reducing the undercooling of the melt. Considering gravity-driven natural convection based on the simulation case in Fig. 2(b), it can be seen from Figs. 2(c) and (f) that both the solute field and temperature field are no longer symmetrical. A mushroom-like solute plume forms along the gravitational direction due to the downward sinking of the heavy solute Cu. Comparing Fig. 2(c) with Fig. 2(b), it can be noted that the growth of the dendrite trunk at the upstream side is promoted while the growth of the dendrite trunk at the downstream side nearly stops, as shown in Fig. 2(c). The growth of the secondary dendrite arms is roughly the same. The dendrite growth anisotropy is significantly different. In general, the dendrite growth dynamics become more complex and the dendrite morphology becomes more diverse under thermal-solute-convection coupling.

Figures 3(a) and (b) quantitatively show the solute concentration and temperature distribution along the vertical symmetric axis of the dendrite under pure solute diffusion, thermal-solute coupling, and thermal-solute-convection coupling, respectively. It can be seen that the solute concentration curves in Fig. 3(a) reveal the same trend for the pure solute diffusion and thermal-solute coupling. The difference lies in the lower dendrite growth rate under thermal-solute coupling, which leads to shorter dendrite trunks comparing to those formed under pure solute diffusion. Under thermal-solute-convection coupling, the solute concentration curve is no longer symmetric. It rises sharply at the solid-liquid interface of the dendrite tips. However, the value is much higher in front of the downstream dendrite tip than that the upper dendrite tip due to the downward sinking of the heavy solute Cu. As for the temperature distribution, it can be illustrated from Fig. 3(b) that when considering the release of latent heat during solidification, the temperature peaks near the center of the dendrite and then decreases. After the addition of natural convection, the maximum temperature value further increases due to the release of a large amount of latent heat as the growth of the dendrite trunk at the upstream side is promoted. This can be confirmed from Fig. 3(c) that the growth rate of the upper-side dendrite tip under thermal-solute-convection coupling is higher than that under thermal-solute coupling.

It is worth mentioning that the starting points of solute concentration curves are the same in all the three cases in Fig. 3(a), while the situation is different for the temperature curves as shown in Fig. 3(b). This is because the thermal diffusion coefficient is generally four orders of magnitude greater than the solute diffusion coefficient in liquid for metallic alloys. In a short period of time, the heat has already diffused to the boundary of the computational domain.

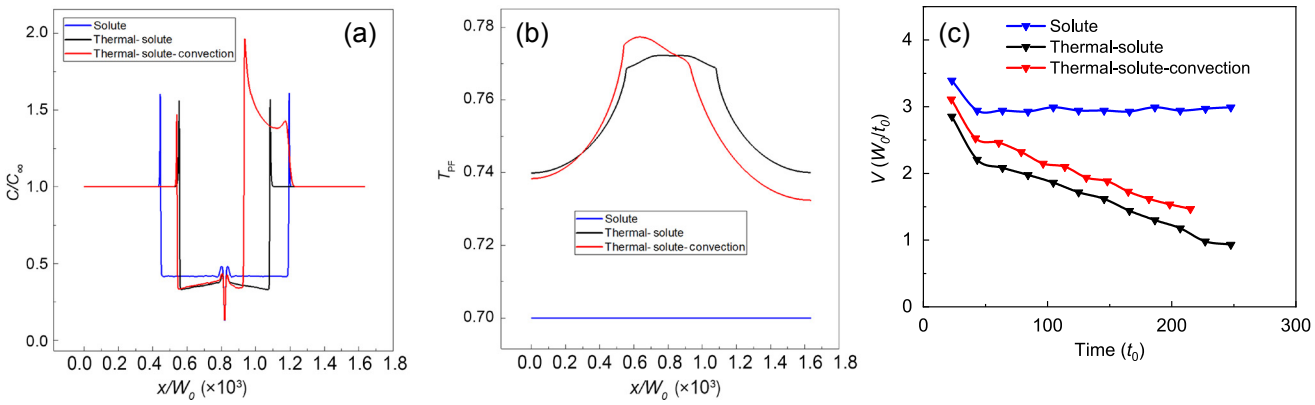

Fig. 3: Solute concentration distribution (a) and temperature distribution (b) along the vertical symmetric axis of the dendrite; (c) growth rate of the upper-side dendrite tip

Since the actual solidification of metal alloys is generally in 3D situation, simulation of 3D dendrite growth under thermal-solute-convection coupling was conducted. With the same dimensionless temperature as the simulation case in Fig. 2, Fig. 4 shows the simulated results of a single 3D dendrite growth in the thermal-solute field under natural convection with a solute expansion coefficient of –0.3. The size of the calculation domain is 409.6×409.6×409.6. It can be seen from Figs. 4(a–c) that the presence of natural convection disrupts the symmetry of the dendrite morphology. However, the difference between the upstream and downstream side is not as pronounced as in 2D case due to the greater freedom and space for thermal-solute-convection transport in 3D case, which can bypass the dendrite backbone [50]. This can also be verified from Figs. 4(d–f), respectively showing the solute, temperature and flow velocity fields. Compared to the 2D case, their difference between the upstream and downstream dendrite tips is less pronounced. It can also be noted from Fig. 4(f) that the downward sinking of the heavy solute Cu increases the flow velocity of the melt, even forming two vortices dispersed on both sides of the downstream dendrite tip.

Further simulation was carried out in which the melt convection was induced in the form of forced convection to compare with the case in Fig. 4. Figure 5 shows a single 3D dendrite growth in the thermal-solute field under forced convection with an inlet flow velocity of 0.02 along the *x*-axis from left to right. The calculation domain size is the same as the simulation case in Fig. 4. It can be noted from Figs. 5(a–c) that forced convection also disrupts the symmetry of the dendrite morphology. The growth of dendrite trunk on the upstream side is promoted, while the growth of the opposite one is inhibited. Similarly, due to the greater freedom and space for thermal-solute-convection transport in 3D case, the difference between the upstream and downstream side is not as obvious as in 2D case. The solute concentration distribution [Fig. 5(d)] and temperature distribution [Fig. 5(e)] are

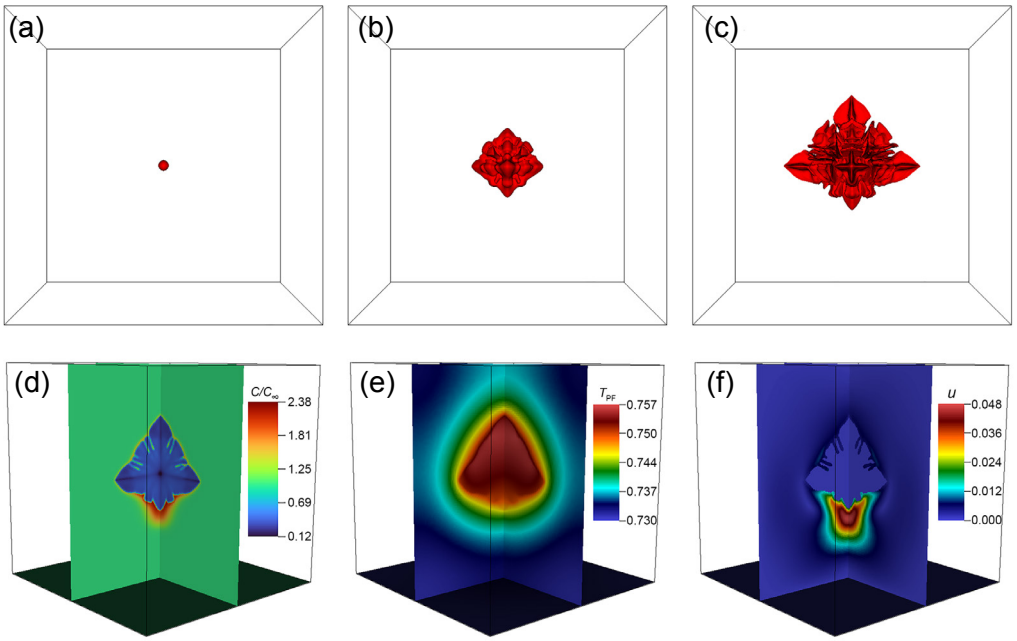

Fig. 4: Simulation of a single 3D dendrite growth in thermal-solute field under natural convection: (a–c) evolution of dendrite morphology after 0, 1,500, and 3,000 time steps, respectively; (d–f) solute, temperature and flow velocity fields corresponding to (c), respectively

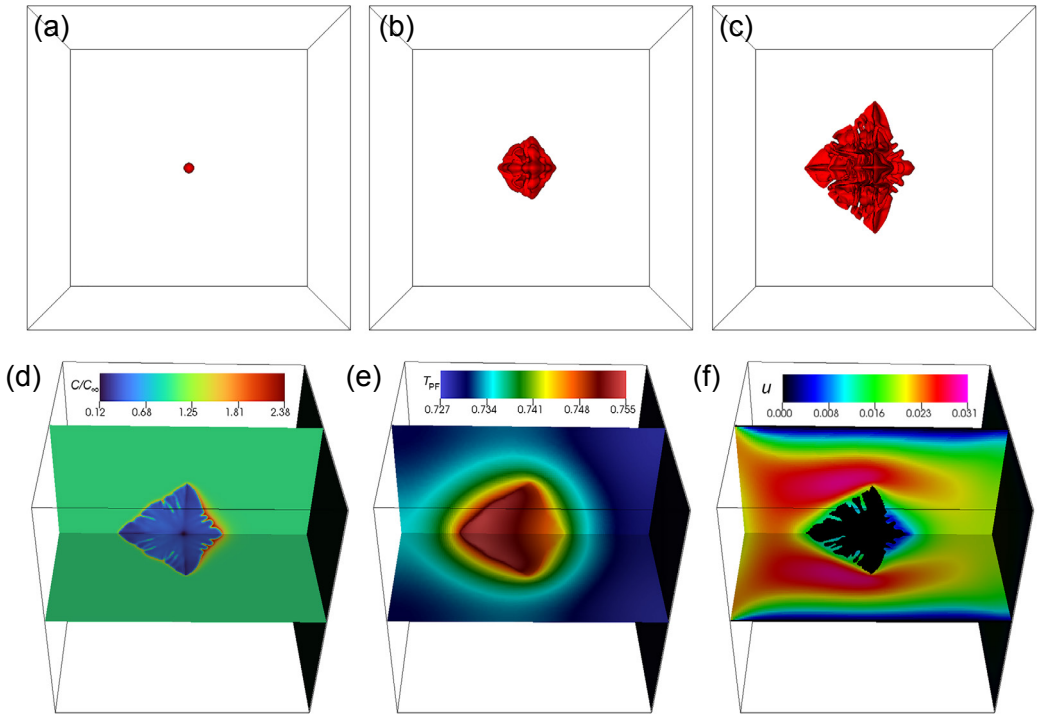

Fig. 5: Simulation of a single 3D dendrite growth in thermal-solute field under forced convection: (a–c) evolution of dendrite morphology after 0, 1,500, and 3,000 time steps, respectively; (d–f) solute, temperature and flow velocity fields corresponding to (c), respectively

similar to those under natural convection in terms of dendrite profiles as illustrated in Fig. 4. The flow velocity under forced convection peaks at the dendrite tips on both sides of the vertical direction.

It can be concluded from Fig. 4 and Fig. 5 that both natural and forced convection alter the dendrite morphology by affecting the solute distribution of the melt. Under natural convection, solute enrichment occurs at the downstream dendrite tip due to the sinking downward of the heavy solute. Under forced convection, the solute discharged from the upstream dendrite tip needs to cross the dendrite tips perpendicular to the flow direction before it reaches the downstream dendrite tip, eventually resulting in significant solute enrichment near the downstream tip.

3.2 Multiple equiaxed dendrite growth

In this section, simulation on multiple equiaxed dendrite growth under thermal-solute-convection coupling was conducted. For comparison, melt convection is still induced in the form of forced and natural convection, respectively. Under forced convection, an inlet flow velocity of 0.01 was set along the x-axis from left to right. A solute expansion coefficient of –0.1 was set under natural convection. In two simulation cases, four seeds with the same growth orientation were randomly located in the calculation domain with a size of 1,638.4×1,638.4. The dimensionless temperature was initially set to 0.7. The simulated results are shown in Figs. 6(a–c) and Figs. 6(d–f), respectively.

It can be seen from Figs. 6(a–c) that when subjected to an inlet melt flow, the growth of dendrite arms on the upstream side is promoted to a certain extent. Meanwhile, there is competitive growth between dendrites C and D [Fig. 6(a)]. The competitive growth mechanism is adjusted by the superposition of their respective solute fields and temperature fields. Especially, solute enrichment occurs in the area between the tips of Dendrites C and D, which significantly slows down the growth rate of dendrites. It can be found from Fig. 6(b) that the highest flow velocity is at the tips of the upper trunk of Dendrite A and lower trunks of Dendrites C and D. This is attributed to the obstruction of dendrites on the melt flow. The intensive solute sweeping effect of the melt flow enhances the growth of the upper trunk of Dendrite A and lower trunks of Dendrites C and D, which incline towards the direction of the melt flow. Due to the release of latent heat during solidification, the middle part of the computational domain has the highest temperature, indicating that the accumulation of dendrites leads to the enrichment of heat in this area, as illustrated in Fig. 6(c).

Under natural convection, it can be seen from Fig. 6(d) that mushroom-like solute plumes form along the gravitational direction due to the downward sinking of the heavy solute Cu. Meanwhile, the growth of the upper trunk of Dendrite D will be inhibited by the solute plume flowing from Dendrites A and B. Unlike forced convection, the area with the highest flow velocity under natural convection is below Dendrites A and B, as shown in Fig. 6(e). This is because the melt flow is induced by the downward sinking of the heavy solute Cu under natural convection. And this area is just located in the superimposed area of solute plumes from Dendrites A and B.

Both natural convection and forced convection change the solute distribution, but they change it in different ways. Under natural convection, the heavy solute continues to

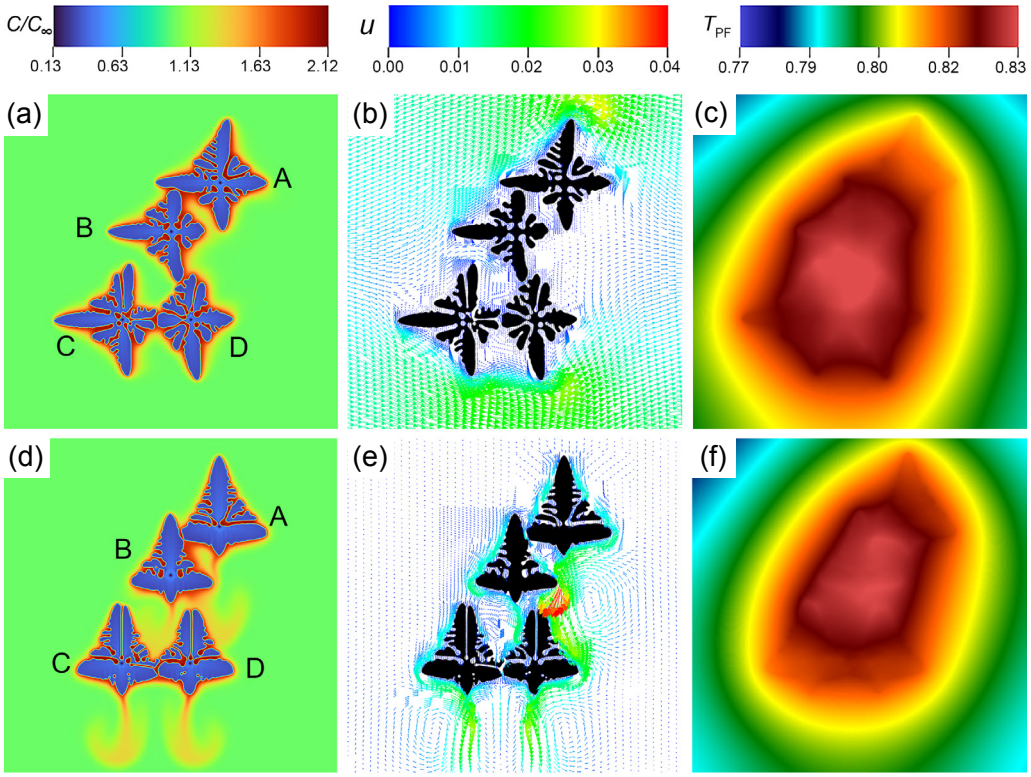

Fig. 6: Simulation on multiple-dendrite growth under thermal-solute-convection coupling: (a–c) solute, flow velocity and temperature fields, respectively under forced convection; (d–f) solute, flow velocity and temperature fields, respectively under natural convection

sink downward due to the constant presence of gravity, even forming vortices in the melt which can facilitate the solute transport. Under forced convection, the solute transported from the upstream side needs to cross the tips of the dendrite trunks perpendicular to the direction of melt flow. Then, the solute accumulates in the melt at the downstream side of dendrites. It should be emphasized that with the growth of dendrites, the intensity of melt flow induced by forced convection will be weaker and weaker due to the obstruction of dendrites. In this case, its role in solute transport will weaken.

An interesting phenomenon appearing both in the two simulation cases is that some trunks of dendrites have split, as shown in Fig. 6. Dendrite tip splitting maybe attributed to the strong convection effect in the melt which weakens the inherent anisotropy during dendrite growth. This effect is known as "convective anisotropy" [33]. By dendrite tip splitting, the dendrite growth tries to adapt to the local thermodynamic condition. In other words, the melt flow not only disrupts the symmetry of dendrite morphology, but also causes dendrite tilting, dendrite tip splitting, etc.

3.3 Columnar dendrite growth

In this section, columnar dendrite growth under solute-thermal-convection coupling was investigated by simulation. Melt convection was induced in the form of natural convection. The gravitational direction was defined always vertical downward, and different columnar dendrite growth directions (along or opposite the gravitational direction) were considered. Therefore, with a calculation domain size of 819.2×1638.4, ten seeds with the same orientation were uniformly arranged at the top and bottom, respectively in two simulation cases. The dimensionless temperature was initially set to 0.3 with a cooling rate of 1×10^{-4}.

Figure 7 shows the columnar dendrite growth while its growth direction follows the gravitational direction with a solute expansion coefficient of –0.04. It can be seen from Fig. 7(a) that the solute begins to accumulate between the dendrite tips and also in the interdendritic liquid. As the solidification proceeds, the solute continues to discharge into the interdendritic liquid and then sink downward. Gradually, the solute moves away from the dendrite tips and bulges are formed at the forefront of the solute streams, as indicated in Fig. 7(b). As the solute continues to move away from the dendrite tips, bulges expand into chimney-like or mushroom-like solute plumes, as shown in Fig. 7(c).

Due to the release of latent heat during solidification, the temperature of the upper part of the calculation domain is higher than that of the lower part. Comparing Figs. 7(d–f) with Figs. 7(a–c), it can be concluded that the thickness of the thermal diffusion layer is significantly greater than that of the solute diffusion layer. This is because the thermal diffusion coefficient is much larger than the solute diffusion coefficient in liquid. However, with the continuous solute enrichment at the dendrite tips and the release of latent heat, the dendrite growth rate continues to slow down. As there is sufficient time for thermal diffusion, the temperature difference between the upper and lower parts of the calculation domain gradually narrows, as illustrated in Figs. 7(e–f).

Figure 8 shows the columnar dendrite growth as its growth direction is opposite to the gravitational direction with a solute expansion coefficient of −0.1. It can be noted from Fig. 8(a) that with the discharge of solute at the solid-liquid interface during solidification, the solute accumulates in the interdendritic liquid. Also, the solute begins to sink, causing the solute concentration in the lower part of the interdendritic liquid phase channels to be higher than that in the upper part. As the solidification proceeds, the solute concentration in the middle and lower parts of the interdendritic liquid channels further increases with the continuous discharge and sinking of solute. Then, the combined effect of release of latent heat and solute enrichment results in the dissipation of the undercooling at the front of the solidification interface. This leads to partial remelting of the middle and lower parts of the columnar dendrites, as shown in Figs. 8(e–f). It is worth noting that since the top and bottom boundaries of the computational domain are subjected to outlet boundaries for the solute field, the total solute content in the computational domain decreases due to the continuous sinking of solute. This even leads to a lower solute concentration in the liquid phase region far from the front of the solidification interface in Fig. 8(c) compared to Figs. 8(a–b). Temperature distribution in Figs. 8(d–f) presents a similar trend as Figs. 7(d–f). The difference is that the temperature distribution opposite to the gravitational direction (Fig. 8) is generally higher than that along the gravitational direction (Fig. 7). This is due to a higher dendrite growth rate in Fig. 8 than in Fig. 7, which consequently results in a larger amount of latent heat release in the melt. The relevant quantitative analysis is shown in Fig. 9.

It can be seen from Fig. 9 that in the initial stage of solidification, the growth rates are basically the same and gradually decrease. The reason for the slower growth rate of columnar dendrites is due to the solute enrichment at the front of the solidification interface and the release of latent heat. However, as the solidification proceeds, the decreasing speeds of the dendrite growth rate in two simulation cases vary a lot. This is attributed to the varying aggregation degrees of solute in the melt at front of the columnar dendrite tips. In the simulation case in Fig. 7, since the columnar dendrites

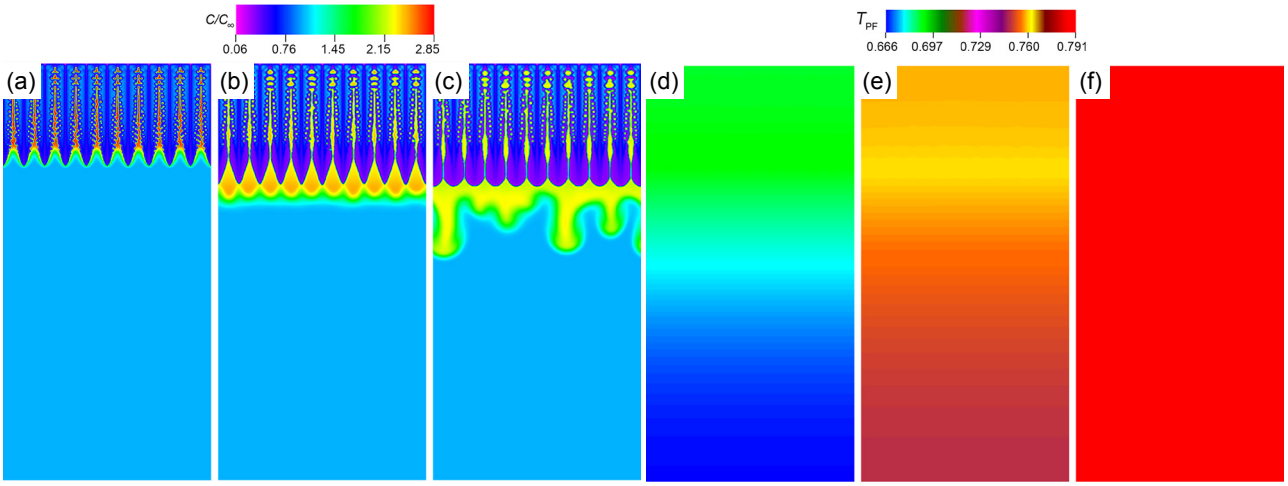

Fig. 7: Simulation on columnar dendrite growth under thermal-solute-convection coupling with the growth direction following the gravitational direction after 4,000, 7,000 and 10,000 time steps from left to right: (a–c) solute field; (d–f) temperature field

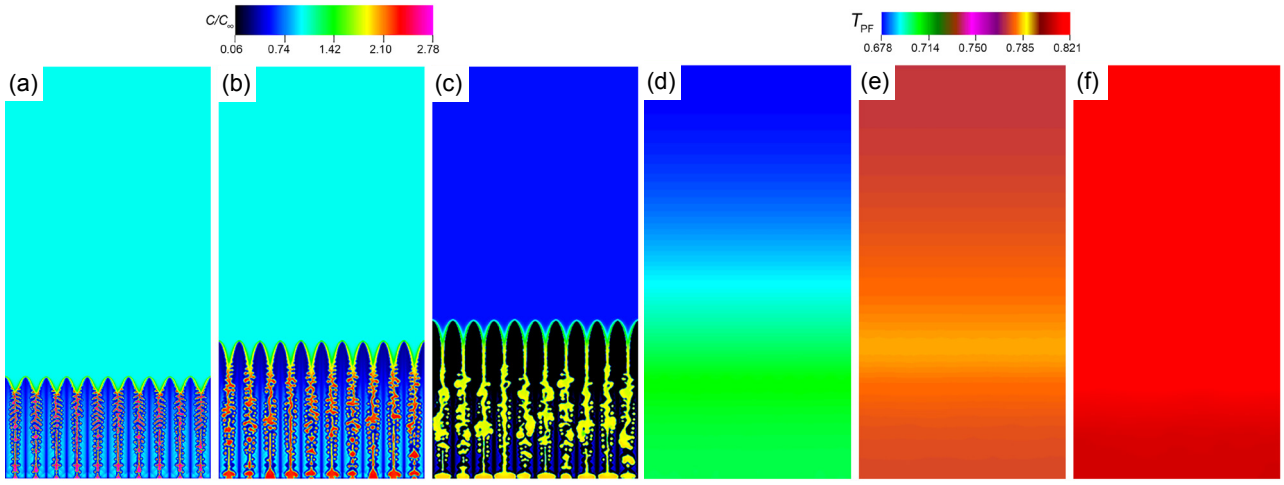

Fig. 8: Simulation on columnar dendrite growth under thermal-solute-convection coupling with the growth direction oppositing to the gravitational direction after 4,000, 7,000 and 10,000 time steps from left to right: (a–c) solute field; (d–f) temperature field

grow along the gravitational direction, the discharged solute gradually sinks downward and accumulates at the columnar dendrite tips. In the simulation case in Fig. 8, the aggregation degree of solute at the columnar dendrite tips is lower when the growth direction of the columnar dendrite is opposite to the gravitational direction.

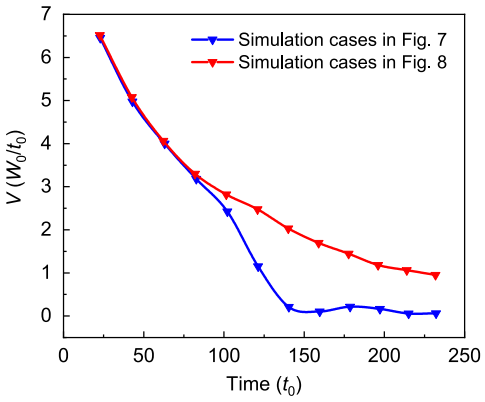

Fig. 9: Variation of growth rate of columnar dendrites versus time, repectively in the simulation cases in Fig. 7 and Fig. 8

4 Conclusions

In the present work, a robust PF-LBM model was developed to investigate the internal relations between various physical fields and their coupling effects on the dendrite growth of Al-Cu alloy. The following conclusions can be drawn:

(1) The release of latent heat during solidification slows down the dendrite growth rate. The thermal diffusion layer is quite thicker than the solute diffusion layer. Both natural and forced convection disrupt the symmetrical growth of dendrites by affecting the solute distribution of the melt near the dendrites. However, they achieve solute transport in different ways.

(2) Dendrite tilting and tip splitting maybe attributed to the strong convection effect in the melt which weakens the inherent anisotropy during dendrite growth. By dendrite tilting and tip splitting, the dendrite growth tries to adapt to the local thermodynamic condition.

(3) When columnar dendrites grow along the gravitational direction, as the heavy solute continues to sink downward and move away from the dendrite tips, bulges expand into chimney-like or mushroom-like solute plumes. When columnar dendrites grow opposite to the gravitational direction, the combined effect of latent heat release and solute enrichment leads to partial remelting of columnar dendrites.

Acknowledgments

This work was financially supported by the National Natural Science Foundation of China (Grant No. 52275370), the Key R&D Program of Hubei Province, China (Grant No. 2022BAD100 and No. 2021BAA048), and the Open Fund of Hubei Longzhong Laboratory, China (Grant No. 2022ZZ-04).

Conflict of interest

The authors declare that they have no conflict of interest.

References

[1] Li X K, Qian W T, Sun K M, et al. Solidification microstructure control of Al-Si-Cu-Ni-Mg alloy and its effect on high temperature tensile properties. Foundry, 2023, 72(5): 545–552. (In Chinese)
[2] Wang Q, Feng K J, Zhang S J, et al. Numerical simulation on fluid flow behavior during 3-dimensional dendrite growth with random preference angle. China Foundry, 2022, 19(5): 387–394.
[3] Huang S C, Glicksman M E. Overview 12-Fundamentals of dendritic solidification-I. Steady-state tip growth. Dynamics of Curved Fronts, 1988, 247–261.
[4] Li Z, Liu Z, Zhao J, et al. Numerical simulation and experimental study of electromagnetic field flow field during solidification of semi solid A356 aluminum alloy under electromagnetic stirring. The Chinese Journal of Nonferrous Metals, 2020, 30(6): 1297–1306. (In Chinese)
[5] Zhang W W, Wang Y Y, Li B, et al. Numerical simulation of flow field temperature field microstructure in electromagnetic continuous casting process of AZ61 magnesium alloy. The Chinese Journal of Nonferrous Metals, 2019, 29(2): 241–247. (In Chinese)
[6] Wu M W, Tian B H, Yang M H, et al. Progress in experimental characterization and simulation of dendrite growth in magnesium alloys. Special Casting & Nonferrous Alloys. 2021, 41(1): 1–10. (In Chinese)
[7] Uchic M D, Groeber M A, Dimiduk D M, et al. 3D microstructural characterization of nickel superalloys via serial-sectioning using a dual beam FIB-SEM. Scripta Materialia, 2006, 55(1): 23–28.
[8] Zietara M, Kruk A, Gruszczynski A, et al. FIB-SEM tomography of 4th generation PWA 1497 superalloy. Materials Characterization, 2014, 87: 143–148.
[9] Beladi H, Rohrer G S. The relative grain boundary area and energy distributions in a ferritic steel determined from three-dimensional electron backscatter diffraction maps. Acta Materialia, 2013, 61(4): 1404–1412.
[10] Ludwig O, Dimichiel M, Salvo L, et al. In-situ three-dimensional microstructural investigation of solidification of an Al-Cu alloy by ultrafast X-ray microtomography. Metallurgical and Materials Transactions A, 2005, 36(6): 1515–1523.
[11] Wang K W, Wu M W, Tian B H, et al. Numerical simulation on dendritic growth of Al-Cu alloy under convection based on the cellular automaton lattice Boltzmann method. Chinese Physics B, 2022, 31(9): 616–627.
[12] Zhang Q Y, Sun D K, Zhang S H, et al. Modeling of microporosity formation and hydrogen concentration evolution during solidification of an Al-Si alloy. Chinese Physics B, 2020, 29(7): 660–668.
[13] George W L, Warren J A. A parallel 3D dendritic growth simulator using the phase-field method. Journal of Computational Physics, 2002, 177(2): 264–283.
[14] Chen C C, Lan C W. Efficient adaptive three-dimensional phase field simulation of free dendritic growth under natural convection. Journal of Crystal Growth, 2010, 312(8): 1437–1442.
[15] Dantzig J A, Di Napoli P, Friedli J, et al. Dendritic growth morphologies in Al-Zn alloys–Part II: Phase-field computations. Metallurgical and Materials Transactions, 2013, 44(12): 5532–5543.

[16] Boettinger W J, Warren J A, Beckermann C. Phase-field simulation of solidification. Annual Review of Materials Research, 2002, 32: 163–194.
[17] Warren J A, Boettinger W J. Prediction of dendritic growth and microsegregation patterns in a binary alloy using the phase-field method. Acta Metallurgica et Materialia, 1995, 43(2): 689–703.
[18] Boettinger W J, Warren J A. The phase-field method: Simulation of alloy dendritic solidification during recalescence. Metallurgical and Materials Transactions A, 1996, 27: 657–669.
[19] Ramirez J C, Beckermann C. Examination of binary alloy free dendritic growth theories with a phase-field model. Acta Materialia, 2005, 53(6): 1721–1736.
[20] Lu Y, Beckermann C, Ramirez J C. Three-dimensional phase-field simulations of the effect of convection on free dendritic growth. Journal of Crystal Growth, 2005, 280(1): 320–334.
[21] Zhang A, Du J L, Meng S X, et al. Three-dimensional thermosolutal simulation of dendritic and eutectic growth. Computational Materials Science, 2020, 171: 109274.
[22] Tönhardt R, Amberg G. Phase-field simulation of dendritic growth in a shear flow. Journal of Crystal Growth, 1998, 194(3): 406–425.
[23] Tönhardt R, Amberg G. Dendritic growth of randomly oriented nuclei in a shear flow. Journal of Crystal Growth, 2000, 213(1): 161–187.
[24] Beckermann C, Diepers H J, Steinbach I, et al. Modeling melt convection in phase-field simulations of solidification. Journal of Computational Physics, 1999, 154(2): 468–496.
[25] Tong X, Beckermann C, Karma A, et al. Phase-field simulations of dendritic crystal growth in a forced flow. Physical Review E, 2001, 63(6): 061601.
[26] Asta M, Beckermann C, Karma A, et al. Solidification microstructures and solid-state parallels: Recent developments, future directions. Acta Materialia, 2009, 57(4): 941–971.
[27] Miller W, Succi S, Mansutti D. Lattice Boltzmann model for anisotropic liquid-solid phase transition. Physical Review Letters, 2001, 86(16): 3578–3581.
[28] Miller W. The lattice Boltzmann method: A new tool for numerical simulation of the interaction of growth kinetics and melt flow. Journal of Crystal Growth, 2001, 230(1): 263–269.
[29] Ohno M, Takaki T, Shibuta Y. Variational formulation of a quantitative phase-field model for nonisothermal solidification in a multicomponent alloy. Physical Review E, 2017, 96(3): 033311.
[30] Zhang A, Meng S X, Guo Z P, et al. Dendritic growth under natural and forced convection in Al-Cu alloys: From equiaxed to columnar dendrites and from 2D to 3D phase-field simulations. Metallurgical and Materials Transactions, 2019, 50: 1514–1526.
[31] Zhang A, Guo Z P, Jiang B, et al. Progress in phase field simulation of alloy solidification structure and pore evolution. The Chinese Journal of Nonferrous Metals, 2021, 31(11): 2976–3009. (In Chinese)
[32] Lan C W, Shih C J. Phase field simulation of non-isothermal free dendritic growth of a binary alloy in a forced flow. Journal of Crystal Growth, 2004, 264(1): 472–482.
[33] Guo Z, Mi J, Xiong S, et al. Phase field simulation of binary alloy dendrite growth under thermal- and forced-flow fields: An implementation of the parallel-multigrid approach. Metallurgical and Materials Transactions B, 2013, 44: 924–937.
[34] Zhang A, Du J, Guo Z, et al. A phase-field lattice-Boltzmann study on dendritic growth of Al-Cu alloy under convection. Metallurgical and Materials Transactions B, 2018, 49: 3603–3615.
[35] Ramirez J C, Beckermann C, Karma A, et al. Phase-field modeling of binary alloy solidification with coupled heat and solute diffusion. Physical Review E, 2004, 69: 051607.
[36] Karma A, Rappel W. Quantitative phase-field modeling of dendritic growth in two and three dimensions. Physical Review E, 1998, 57: 4323–4349.
[37] Zhang X, Kang J, Guo Z, et al. Development of a Para-AMR algorithm for simulating dendrite growth under convection using a phase-field-lattice Boltzmann method. Computer Physics Communications, 2018, 223: 18–27.
[38] Karma A. Phase-field formulation for quantitative modeling of alloy solidification. Physical Review Letters, 2001, 87: 115701.
[39] Guo Z, Xiong S M. On solving the 3-D phase field equations by employing a parallel-adaptive mesh refinement (Para-AMR) algorithm. Computer Physics Communications, 2015, 190: 89–97.
[40] Girimaji S. Lattice Boltzmann method: Fundamentals and engineering applications with computer codes. AIAA Journal, 2013, 51(1): 278–279.
[41] Krüger T, Kusumaatmaja H, Kuzmin A, et al. The lattice boltzmann method: Principles and practice. Cham: Springer, 2017.
[42] Takaki T, Rojas R, Sakane S, et al. Phase-field-lattice Boltzmann studies for dendritic growth with natural convection. Journal of Crystal Growth, 2017, 474: 146–153.
[43] Tian B H, Wu M W, Zhang A, et al. Phase-field modeling of dendritic growth of magnesium alloys with a parallel-adaptive mesh refinement algorithm. China Foundry, 2021, 18(6): 541–549.
[44] Zhang A, Jiang B, Guo Z P, et al. Solution to multiscale and multiphysics problems: A phase-field study of fully coupled thermal-solute-convection dendrite growth. Advanced Theory and Simulations, 2021, 4(3): 2000251.
[45] Karma A, Tourret D. Atomistic to continuum modeling of solidification microstructures. Current Opinion in Solid State and Materials Science, 2016, 20(1): 25–36.
[46] Zhang A, Guo Z, Xiong S. Eutectic pattern transition under different temperature gradients: A phase field study coupled with the parallel adaptive-mesh-refinement algorithm. Journal of Applied Physics, 2017, 121: 125101.
[47] Sun D K, Chai Z H, Li Q, et al. A lattice Boltzmann-cellular automaton study on dendrite growth with melt convection in solidification of ternary alloys. Chinese Physics B, 2018, 27: 088105.
[48] Zhang Q Y, Sun D K, Pan S Y, et al. Microporosity formation and dendrite growth during solidification of aluminum alloys: Modeling and experiment. International Journal of Heat and Mass Transfer, 2020, 146: 118838.
[49] Zhu C S, Li T Y, Zhao B R, et al. Simulation of inclined dendrites under natural convection by KKS phase field model based on CUDA. China Foundry, 2023, 20(5): 432–442. https://doi.org/10.1007/s41230-023-2128-0.
[50] Jeong J H, Goldenfeld N, Dantzig J A. Phase field model for three-dimensional dendritic growth with fluid flow. Physical Review E, 2001, 64: 041602.